Automatic quantification of intravascular optical coherence tomography

Wang, A.

CHAPTER

4

3D assessment of stent cell size and side branch access in intravascular optical coherence tomographic pullback runs

This chapter was adapted from:

3D assessment of stent cell size and side branch access in intravascular optical coherence tomographic pullback runs

Ancong Wang, Jeroen Eggermont, Niels Dekker, Patrick J.H. de Koning,

Johan H.C. Reiber, Jouke Dijkstra

Computerized Medical Imaging and Graphics. 2014,
Volume 38, Issue 2, Pages 113-122.

Abstract

We present a semi-automatic approach to assess the maximum circular unsupported surface area (MCUSA) of selected stent cells and the side branch access through stent cells in intravascular optical coherence tomography (IVOCT) pullback runs. Such 3D information may influence coronary interventions, stent design, blood flow analysis or prognostic evaluation. First, the stent struts are detected automatically and stent cells are reconstructed with users' assistance. Using cylinder fitting, a 2D approximation of the stent cell is generated for MCUSA detection and measurement. Next, a stent surface is reconstructed and stent-covered side branches are detected. Both the stent cell contours and side branch lumen contours are projected onto the stent surface to indicate their areas, and the overlapping regions are measured as the side branch access through these stent cells. The method was evaluated on phantom data sets and the accuracy of the MCUSA and side branch access was found to be 95% and 91% respectively. The usability of this approach for clinical research was proved on 12 in vivo IVOCT pullback runs.

4.1 Introduction

Over Coronary stents are widely used in the treatment of coronary artery disease. During a percutaneous coronary intervention (PCI), a stent is delivered to a stenosis and extended by inflating a balloon to keep it open. Clinical research has demonstrated that the support of an implanted stent to the vessel wall positively influences the outcome of the PCI [1-3]. Given these positive results, there is an increasing demand from clinical researchers for detailed stent analysis. However, the past research on the stent support mainly focused on the 2D stent struts distribution in cross-sectional images, such as the stent contour area, the number of visible struts and the inter-strut angle in a single frame [4-6]. Recently, 3D assessment like the size of every stent cell [7-9] has become popular for stent analysis. Stent cell size assessment may be used to evaluate the actual stent designs with respect to the struts distribution [10-12] or even the mechanism of controlled drug release from drug-eluting stents [13]. As a new desired feature, the maximum circular unsupported surface area (MCUSA) of stent cells was proposed to describe the support to the vessel wall [14;15]. It was defined as the maximal circular area that can be fit inside a 2D approximation of a stent cell.

Stents with smaller cells usually provide better support to the vessel wall, but when a stent covers a side branch, small stent cells in front of the side branch may lead to restenosis or obstruction of the blood flow to the side branch due to bridging [16-18]. If necessary, a stent cell in front of the side branch can be expanded by a second balloon to enlarge its ostium, but it may lead to stent fracture [19;20]. For interventional cardiologists, assessing the side branch access through stent cells may assist the PCI treatment prognosis of stent-covered side branches and the stent design evaluation.

To measure stent cells accurately, a precise description of the stent position is necessary. As a relatively new 3D optical imaging technique, intravascular optical coherence tomography (IVOCT) is increasingly being used to evaluate in-vivo coronary lesions [21;22]. It provides very high resolution (about 10 μm) cross-sectional images of coronary arteries so that the stent measurement can benefit from it. In IVOCT pullback runs, the implanted stents are visible as individual bright spots (struts) with a black shadow behind them [23;24]. Fig. 1 presents two in-vivo IVOCT images in Cartesian coordinate system and polar coordinate system separately.

In this paper, we present a semi-automatic approach to assess the MCUSA of every selected stent cell and the side branch access through stent cells. The details of the method are presented in section 2, while the validation method and the empirical results from a phantom data set and twelve in-vivo IVOCT pullback runs are presented in section 3 and section 4. The analysis of the results is given in section 5 and the conclusions and future work in section 6.

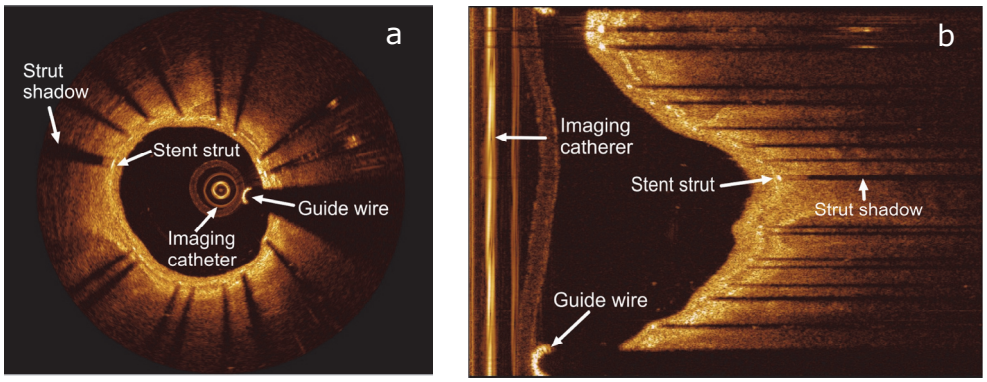

Figure 4-1. Two examples of in-vivo IVOCT images with an implanted stent. Figure (a) shows a Cartesian image, while figure (b) shows the corresponding polar image. In both images, a stent strut, the shadow behind this stent strut, the guide wire and the imaging catheter are annotated.

4.2 Methods

The presented methodology consists of six main steps: (1) automatic stent strut detection; (2) semi-automatic stent cell contour reconstruction; (3) 2D stent cell approximating and MCUSA assessment; (4) irregular stent surface reconstruction; (5) stent-covered side branch detection; (6) assessment of the side branch access through stent cells. A flow chart of the methodology is shown in Fig. 2. More details are given in the following sections.

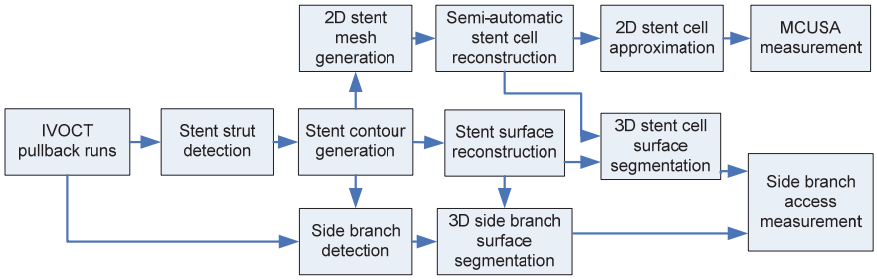

Figure 4-2. The flow chart of the presented method for MCUSA and side branch access measurement.

4.2.1 Stent strut detection

Before measuring the MCUSA and the side branch access, we need to reconstruct stent cells. The strut positions are needed because stents appear as struts in IVOCT pullback runs. Stent struts can be manually detected but it will be very time-consuming and lack of reproducibility. Several (semi-)automatic strut detection methods have been published [6;23-26]. In this manuscript, our recently published automatic stent strut detection method was used [23]. It segments the struts and the guide wire in polar IVOCT pullback runs automatically. This method was validated using almost 20000 struts under different conditions (malapposed, apposed and

covered) in 10 various quality in-vivo pullback runs, and the method has demonstrated that about 94% of the stent strut can be automatically detected.

4.2.2 Stent cell reconstruction

Without enough a-priori information, it is challenging to recognize a stent cell fully automatically, as different stents have different cell structures and their shapes can be distorted during the implantation. Additionally, if a stent cell in front of a side branch has been extended for better blood access, its shape and size will be greatly different from the other stent cells. Due to the irregular stent shapes and variable cell structures, automatic stent cell reconstruction methods may have limited performance. To come up with an accurate and maximally robust technique, we have decided for a semi-automatic stent cell reconstruction method, whereby users are requested to observe the stent cell pattern and confirm the struts belonging to a particular stent cell by manual interaction.

This means that the user needs to click on the struts belonging to a single stent cell in 2D space. Although users can observe stent cell structures in 3D space as Fig. 3(a) shows, these structures are not very clear due to the illusion of perspective projection. Besides, it is difficult for user to click struts in 3D space. To simplify the user observation and interaction, the stent is cut up along the longitudinal direction and opened as a 2D mesh. To do this, the stent contour center in each frame is required as the first step. As shown in Fig. 1 (a), the cross section of the implanted stent is elliptical, so it is reasonable to fit an ellipse to the stent struts as the approximation of the stent contour. Here, a least-square method [27] is chosen to fit the ellipse. In some frames, there are not enough struts for an accurate ellipse fitting result. Under such circumstances, struts from neighboring frames are projected to the current frame for ellipse fitting as well, because the stent contour position does not change much between two neighboring frames. In case there are still not enough stent struts available (typically < 6), the stent contour in this frame will be linearly interpolated from the neighboring stent contours. The fitted ellipses are first used to remove the outliers from the struts detected in section 2.1. All the struts are checked by computing their distance to the elliptic stent contour. If a strut is located too far away from the ellipse, it will not be used for the stent surface reconstruction.

After the elliptical stent contours are fitted, an imaginary cylinder is created along the centerline of the pullback run with the diameter being the average length of all ellipse axes. The struts in the individual frames are shifted until the stent center overlays the original Cartesian image center. Next, all the stent struts are projected onto this cylinder along a ray shot from the image center; Fig. 3 (b) shows an example of a projection result. This step guarantees that there will be no overlaid struts during the projection. When the cylinder is opened into 2D, the stent is converted to a 2D mesh (Fig. 3 (d)). This 2D mesh is only used to simplify the users' observation and interaction, but not for stent cell size measurement; for this reason, a mapping is kept between the 2D struts and the original 3D struts. Later in section 2.6, the detected side branch lumens are also projected onto this imaginary cylinder and opened together with the stent, so that the stent cells which may be in front of side branches could be detected easily as Fig. 3 (d) shows.

Users are requested to observe and recognize stent cells in the 2D mesh, and then click on the struts belonging to a stent cell in the proper order. When a strut is indicated in the 2D mesh, the corresponding original 3D strut position is found based

on the known mapping between 2D and 3D struts. The time required for this interactive process depends on the stent structure complexity and the number of struts. Typically, it takes about 15 seconds to indicate all the struts belonging to a stent cell. Next, the stent cell contour is generated by linking the 3D struts in the proper order using a natural-spline. An example of a reconstructed stent cell contour is presented in Fig. 3(e).

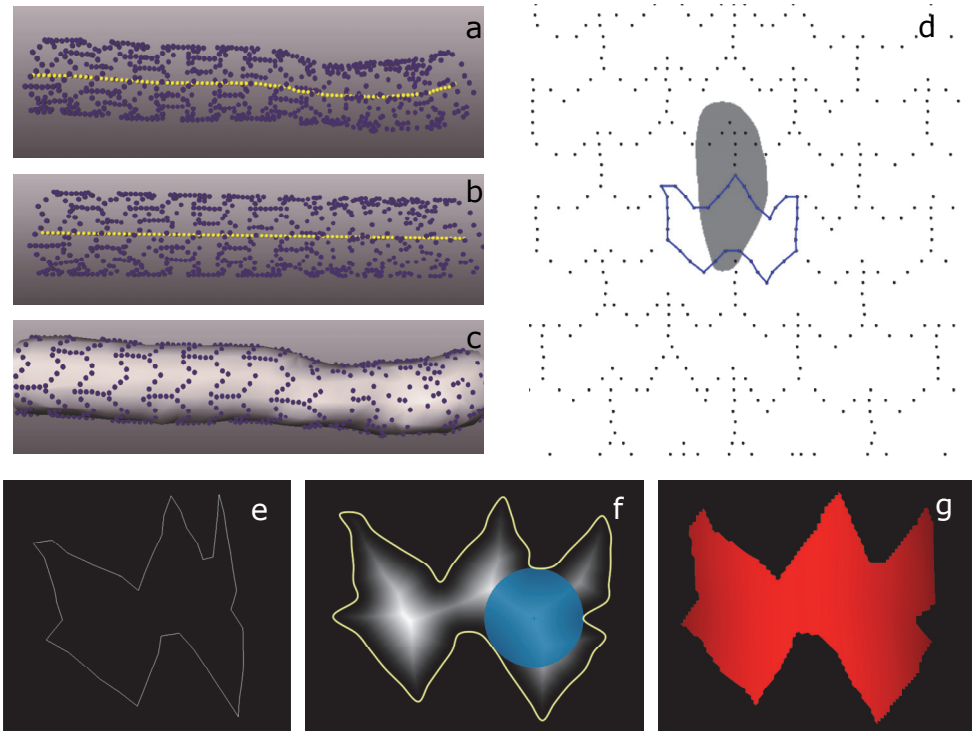

Figure 4-3. (a) Elliptic stent contours are fitted to the original stent struts (blue dots) from an in-vivo IVOCT pullback run. Based on the ellipse centers (yellow dots), (b) struts are shifted and projected onto a cylinder. (c) An irregular stent surface is reconstructed from the original struts. (d) The stent is opened into 2D and the struts are presented as black dots, while a user detected stent cell is presented in blue. Similarly, a side branch lumen (gray area) is also projected onto the cylinder and opened to show its relative location with respect to the stent cells. (e) A 3D stent cell is reconstructed according to the 2D/3D struts mapping. The cell contour is generated by linking struts with a natural spline. (f) A 2D approximation of the stent cell is given and the grey value inside the contour is the distance transform result. Its MCUSA (the blue circular area) is detected by searching for the highest intensity pixel in it. (g) The cell contour is projected onto the stent surface to determine the cell surface for the further side branch access assessment.

4.2.3 MCUSA estimation

The MCUSA of a stent cell is the maximum circular area inside this stent cell. As a 3D structure, every stent cell needs a 2D approximation to compute its MCUSA. This

approximation should preserve the main stent cell size and shape details. It can be generated by fitting a regular shape to the stent cell and opening into 2D. In the case of a stent, the logical choice for the regular shape is a cylinder. Fitting the whole stent to a single cylinder could introduce errors, because stents are bended and distorted during the implantation procedure e.g. at side branches (Fig. 3 (a)). In order to minimize the introduced errors, a cylinder side surface is fitted to only the struts belonging to a single stent cell instead of all the struts. The fitting is based on a least-squares cylinder fitting method [28], which minimizes the error between struts and the fitted cylinder side surface. The initial orientation of the cylinder is set as the longitudinal direction of the pullback run and the initial radius is the average length of the stent ellipse axes. After the cylinder fitting, the stent struts are projected onto the fitted cylinder and opened into 2D. Struts are linked by a natural spline as Fig. 3 (f) shows. Before opening, a connectivity check is applied to make sure that stent cell cannot be split into two halves. If a stent cell could be split, the opening position of the cylinder will be rotated to the outside of the stent cells.

The largest circle which can be found inside this 2D approximation is the MCUSA. The center of the MCUSA is the point which has the maximum shortest distance to its surrounding boundary. To detect this point, first a binary image is generated from the 2D approximation. Next, the distance transform algorithm [29] is applied to this binary image. In the resulting image, the pixel with the highest intensity defines the center of the MCUSA and its intensity value is the radius of the MCUSA. An example is given in Fig. 3 (f). Please note that although there may be more than one maximum circle, they all have the same size.

4.2.4 Stent surface reconstruction

As Fig. 5 (a) presents, the side branch access through a stent cell can be measured by computing the overlaid region between the side branch and the stent cell. To achieve the common region between them, we need to reconstruct a precise stent surface for the implanted stent. The stent cell surface and the side branch lumen surface will be segmented on the stent surface. During the stent extension, the balloon cannot evenly expand in all areas because the hardness of tissue and plaques is different. Therefore, the shape of the implanted stents is irregular in general. In our approach, a precise and piecewise smooth stent surface is reconstructed from the detected stent struts using Hoppe's method[30]. The surface consists of many tiny triangles. This method requires a group of relatively evenly distributed points and has two parameters: the neighborhood size and the sample spacing. The first parameter is the average neighbor number of each strut which is used to estimating the local surface orientation. Here, it depends on the average number of struts in each frame. The second parameter is used to specify the spacing of the 3D sampling grid. An example of the reconstructed stent surface is shown in Fig. 3 (c).

If a guide wire is used during the IVOCT image acquisition, it blocks all the information behind it including stent struts. Missing struts due to the guide wire shadow will cause breaches and distortion on the reconstructed stent surface. To solve this problem, imaginary struts are added behind the guide wire on the elliptical stent contours. Different locations of the imaging catheter and the guide wire result in different size of guide wire shadows. To estimate the possible number of blocked struts, we deduce the angle of the blocked arcs based on the guide wire shadow edges detected in section 2.1. On the covered ellipse arc, an imaginary strut is added every 30

degrees. A special mark is given to these imaginary struts, because they will be only used for the stent surface reconstruction, but not for stent cell reconstruction.

4.2.5 Side branch detection

To measure the side branch access through stent cells, the stent-covered side branches need to be detected. In IVOCT pullback runs, a side branch appears like a black lacuna on the main vessel lumen. Therefore, it can be detected by checking the distance changing from the lumen center to the lumen boundary. If the distance profile shows a sharp increase in a certain region, it could indicate the presence of a side branch. Because the centers of Cartesian IVOCT images represent the imaging catheter positions but not the lumen centers, the lumen centers have to be detected first. In the typical situation where a stent is well extended to support the vessel wall, the stent contour center can be treated as an approximation of the lumen center. In this research, only the side branches which are covered by apposed or covered stents are analyzed, therefore, the ellipse centers from section 2.2 were used.

As demonstrated in Fig. 4 (a), the image catheter and the guide wire are present between the lumen center and the lumen boundary. Before the distance is computed, these bright regions have to be masked out. During the IVOCT imaging acquisition, the imaging catheter generates bright vertical lines in the polar images. With a proper z-offset correction, the artifacts are located in the same position during the whole pullback run. Therefore, these are detected by applying a dynamic programing algorithm to the whole pullback run in the longitudinal direction and later masked out. The guide wire has been detected during the strut detection [23], so they are masked out as well. After masking, the polar IVOCT images are converted into Cartesian images and a median filtering is applied followed by a Gaussian smoothing to smooth the bright tissue region. To specify the lumen region, images are converted into binary images by thresholding the intensity values. The threshold is computed based on the histogram of the whole image. An example of a binary image is presented in Fig. 4 (b).

The distance from the center to the lumen boundary is measured every half degree and Fig. 4 (c) shows the distance profile of a single frame. The side branches and the guide wire result in the two peaks with sharp increasing and decreasing in the profile. As the automatic stent strut detection also detects guide wire besides the stent struts [23], peaks resulting from guide wire will be ignored. After removing the guide wire peaks, the highest peaks in the profile indicate the possible side branch positions. Four main rules are used to identify a side branch: 1) the distance is longer than the median value of all the distances in each frame; 2) this region starts and ends with significant distance changes; 3) the width of this region is at least 30 degrees; and 4) a candidate side branch should have a reasonable size in the longitudinal direction. If a candidate side branch is found, its start and end points will be detected by computing the biggest changes of the distance. Next, the start and the end of each side branch are marked out as Fig. 5 (b) shows. The side branch lumen contour is generated by linking these starts and ends with a natural spline. We also noticed that in a few cases, the struts in front of a side branch were covered by tissue composing a bridge over the side branch. In these cases, a manual correction could be needed.

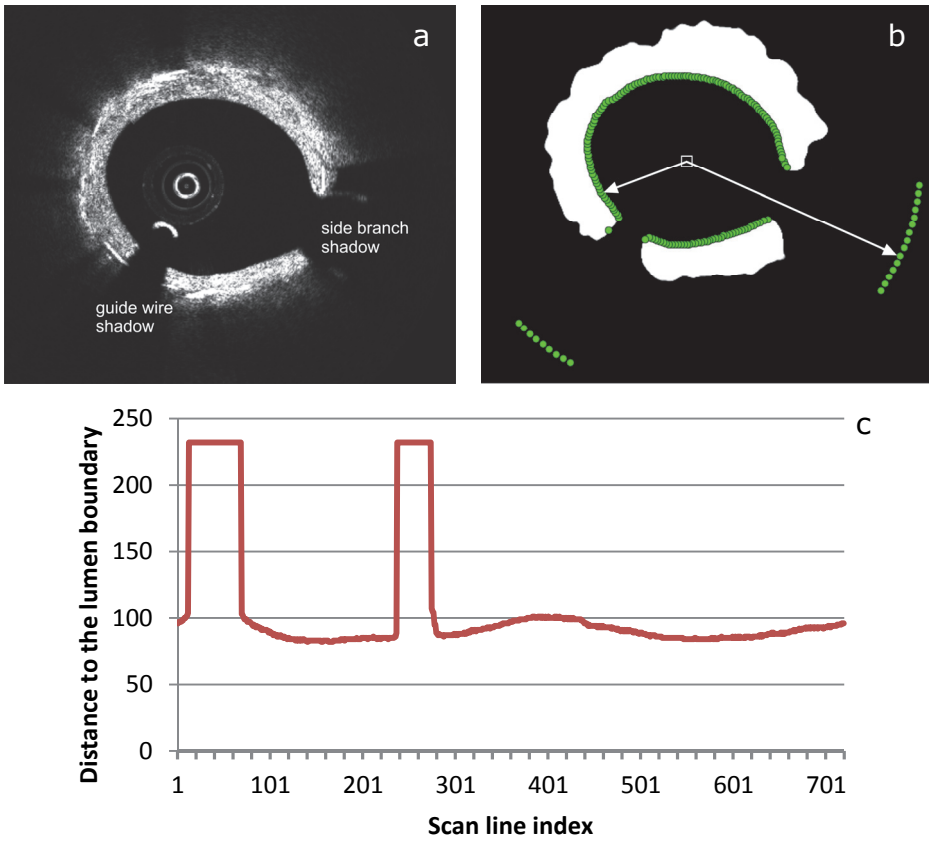

Figure 4-4. (a) presents an in-vivo IVOCT image with a side branch and a guide wire. After processing, the image result is shown in figure (b). From the fitted ellipse center (the small white square in the middle), the distance to the lumen contour is computer over all 360 degrees. The scan-line ends at the lumen contour or the image edge with green dots. The profile of this distance is presented in figure (c). There are two peaks in the profile which represent the side branch and the guide wire respectively.

4.2.6 Side branch access measurement

In this paper, the side branch access through a stent cell is defined by the ostium which is generated by the stent cell above the side branch. As Fig. 5 (a) presents, the side branch access through a stent cell is measured by computing the overlaid region between stent cells and side branches. Since the stent surface has been reconstructed, both stent cell areas and side branch areas can be segmented on it.

Here, the stent cell contour is used for this segmentation. Because the stent cell contour is generated by linking struts using a natural spline, the interpolated part may not be exactly located on the stent surface. For accuracy, the cell contours are projected onto the stent surface to segment the 3D stent cell surfaces. As the stent cell contours are almost located on the stent surface, a simple linear extrusion is used for performance issues. The cell contour is extruded toward to the stent center; thereby

generating a hollow object which intersects with the stent surface as Fig. 5 (d) shows. The contour extrusion direction and length is set by a vector which is orthogonal to the centerline of the stent and passes through the center of the bounding box of the stent cell. The collision part is segmented from the stent surface resulting in the 3D cell surface as Fig.3 (g) shows. This cell surface comprises many small triangles and its size is the sum of the areas of these triangles.

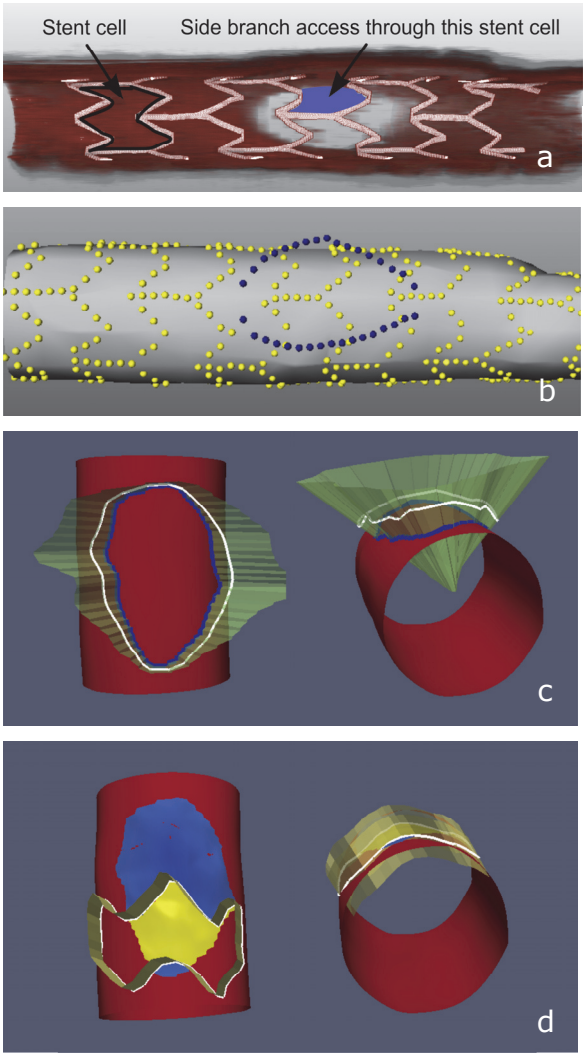

Figure 4-5. (a) A stent covers a side branch. The black contour indicates a stent cell. The side branch appears as a hole on the red vessel wall. The blue area shows the side branch access through a stent cell. (b) shows the struts (yellow dots), the side branch lumen contour (delineated by blue dots) and the fitted stent surface (light grey). (c) The 3D side branch lumen contour (white) is located far away from the stent surface (red), and the blue contour is the projection result. (d) The stent cell contour (white) is almost located on the stent surface. The linear extrusion of the contour (green) generates the contour projection (white) to segment the access area (yellow) on the side branch lumen surface (blue).

Stent cell structures are easily observed in the 2D stent mesh. If the stent-covered side branch lumen is shown together with the 2D mesh, the stent cells that may be in front of this side branch can easily be detected. This could speed up the manual interaction. To do this, the side branch contour is projected onto the same imaginary cylinder for stent cell contour detection in section 2.2 and opened into 2D as Fig. 3 (d) shows. The side branch lumen contour is projected onto the stent surface to segment the side branch lumen area. Unlike stent cell contour projection, side branch lumen

contours usually are located further away from the stent surface as Fig. 5 (b). If they are extruded linearly, the results will contain large errors. Therefore, an accurate projection method is used for side branches. Since the side branch contour surrounds the cylindrical stent surface, each point on the side branch contour should be projected toward to the lumen center. Practically, each point on the lumen contour shoots a ray to the lumen center in the same longitudinal position. The intersected points between the rays and the stent surface are linked using a natural spline to segment the side branch lumen surface. An example is shown in Fig. 5 (c). As the stent cell surfaces and the side branch lumen surfaces are all segmented from the stent surface, the overlaid part between a stent cell surface and a side branch lumen surface represents the side branch access through this stent cell. An example is given in Fig. 5 (d).

4.3 Validation method

For in-vivo stents, the ground truth of their stent cell size and the side branch access through stent cells are not available. Because first, the implanted stents cannot be removed from the patients, and second, the irregular stent surface is not suitable for validation, because it is almost impossible to achieve its ground truth. To validate the new presented methods, a phantom data set was created by scanning a 3.0 mm × 8.0 mm coronary stent using Micro CT. As Fig. 6 (a) shows, in the CT data set, the stent is visible as struts similar in IVOCT pullback runs. Besides, although Micro CT can scan only small objects, it provides a higher resolution than IVOCT (30 times higher than IVOCT in the longitudinal direction). The phantom size is 1024 pixels × 1024 pixels × 1240 frames with a voxel size of 5.86 μm × 5.86 μm × 6.62 μm. Therefore, Micro CT data sets were used for the presented method validation and the stent cell contours generated from the phantom data set are accurate enough to be treated as the ground truth, as Fig. 6 (b) presents. Without any resistance from the vessel wall, the stent was extended evenly and can thus be treated as a cylinder. Although this is not the situation for a real stent inside a patient, it allows us to validate the method itself without potential measuring errors resulting from an irregular stent surface. By projecting the stent cell contours onto the stent cylinder, the ground truth of the stent cell size can be estimated.

The extended stent was found to be 3.1 mm × 8.2 mm; therefore it was represented by a cylinder of the same size. All the struts in the phantom data set were detected and the stent cells were reconstructed. Next, every stent cell contour was projected onto the cylinder and opened into 2D. The size of these opened stent cell surfaces were recorded as the ground truth of the stent cell surface size. At the same time, the ground truth of the MCUSA of every stent cell was computed as well. Since the phantom data set contains no side branches, four ellipses were generated as virtual side branches outside the stent cylinder surface. Each ellipse has a different position and orientation. Side branch surfaces were segmented by projecting all the ellipses onto the stent cylinder and opened into 2D as Fig. 7 (a) shows. Compared with the stent cell surfaces, the ground truth of the side branch access through stent cells can be measured by the common areas (Fig. 7 (b)).

To evaluate the accuracy of the proposed method, the stent should be scanned in a phantom by an IVOCT system and a Micro CT system. However, we did not have a proper phantom which was both IVOCT and micro-CT compliant. Therefore, the CT data set was resampled to simulate the in-vivo IVOCT data set. In our in-vivo IVOCT

pullback runs, the voxel size is 6.85 μm × 6.85 μm × 200 μm. Therefore, the original phantom data set was re-sampled by selecting 1 frame out of every 30 frames, resulting in the similar resolution as IVOCT pullback runs (5.86 μm × 5.86 μm × 200 μm) as Fig. 6 (c) shows. The re-sampled phantom data set was processed by the presented approach and the results were compared with the ground truth for validation. Besides, the accuracies of 2D stent cell approximations and stent cell surfaces segmented from stent surface were also validated as essential pre-steps.

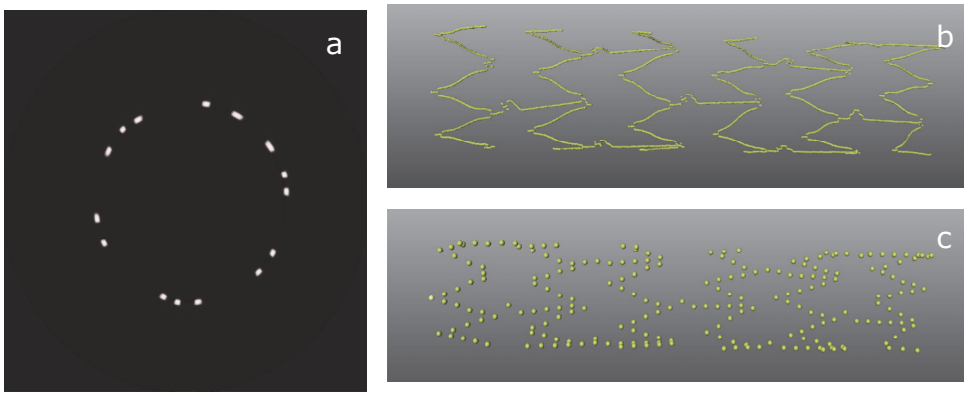

Figure 4-6. (a) a single Micro CT frame with stent struts (white points), which looks similar to clinical IVOCT images. In both figures, the stent struts appear as bright spots. (b) half of the struts detected in the original phantom data set and (c) half of the struts detected in the re-sampled phantom data set. There are much more struts in the original phantom data set than the re-sampled data set and its cell contour can be treated as the ground truth.

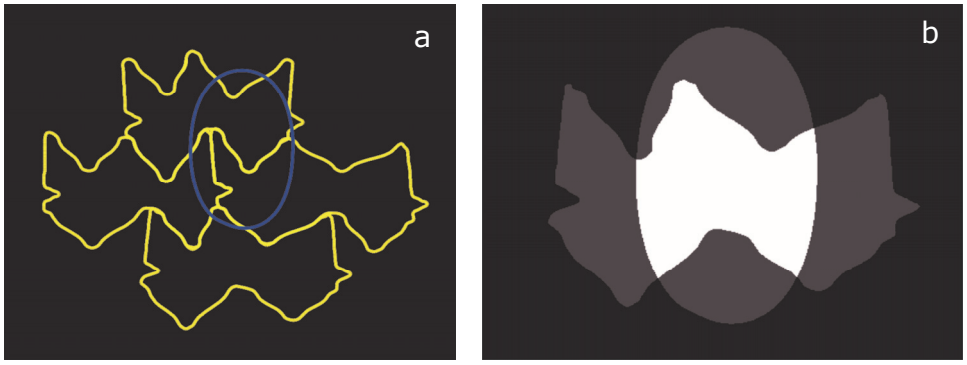

Figure 4-7. (a) The opened 2D stent cells (yellow) in the original phantom data set and an opened imaginary side branch lumen (blue). (b) An example of a side branch access through the stent cell from the original phantom data set. The brightest region in the image is the side branch access to the main vessel through this stent cell.

To examine the usability of this approach on clinical data sets, a total of 12 randomly selected IVOCT pullback runs from a one-year follow up study were used. They were acquired with a C7-XR OCT intravascular imaging system (LightLab, Westford, MA, USA). Their resolution is 6.85 μm × 6.85 μm × 200 μm. Ten pullback runs contained 271 frames using a pullback speed of 20 mm/s, while the other two contained 541 frames with speed of 10 mm/s. Nine data sets were acquired with a guide wire, while the others contain no guide wire. All the stents were drug-eluting stents, except for one bioresorbable vascular scaffold (BVS). They contained a total of 726 recognizable stent cells and 27 side branches were located in the stented regions. Because of the IVOCT image quality and guide wire shadows, not all of the stent cells and side branches could be measured. From the measureable stent cells, we randomly selected 105 stent cells for subsequent testing. The 3D stent cell surface and the corresponding 2D stent cell approximation should have similar size. Some of the stent cells in front of the side branch had been extended, so we also checked whether their full cell size and the MCUSA are reasonable bigger than the other stent cells. For stent-covered side branches, extended stent cells should offer a bigger access than unextended stent cells. Therefore, the average percentage of the biggest side branch access through stent cells was computed.

As Figure 3 (d) shows, the stent cells in the 2D mesh are very clearly visible, so we expected the stent cell results from different experts to be the same. Therefore, the assessment of the inter/intra-operator variability is not considered in this research. One trained expert selected and reconstructed all the stent cell contours and side branch lumen contours as the ground truth.

4.4 Results

Table 1 presents the full stent cell size and the MCUSA size results from both original and re-sampled phantom data sets. For 12 in-vivo IVOCT pullback runs, the results are given in Table 2. Comparisons of the 3D stent cell surface and the 2D stent cell approximation in both original and re-sampled phantom data sets are shown in Figure 8.

The side branch access measurement results in all original CT data set, re-sampled CT data set and in-vivo IVOCT data sets are given in Table 3. According to the results, the average size of side branches was 1.2 ± 0.8 mm^2, and each side branch was covered by 1.7 ± 0.8 stent cells. The average side branch access through each stent cell was 0.7 ± 0.5 mm^2. Fifteen of the side branches were covered by only one stent cell, so no stent wire would block their entrances. Eight of the side branches were covered by two stent cells. Three side branches were covered by three stent cells and one by six stent cells.

The automatic strut detection method was developed using the MeVisLab toolbox 2.2 (MeVis Medical Solutions AG, Bremen, Germany) and VTK toolkit 5.10 (www.vtk.org) together with in-house developed C++ modules. For processing, we used Windows 7 Professional x64 Edition with a 2.0 GHz CPU and 4 GB of memory. Generally, it takes less than 1 minute to detect all the stent struts in a pullback run of 271 frames. The semi-automatic stent cell reconstruction costs about 10 seconds for every stent cell, while the other processing usually takes about 1 minute. If implemented using pure C++ code, the computing time could be further shortened. The whole processing time depends on the length of the stent and how many stent cells need to be measured.

Table 1. The maximum, minimum, mean value (with standard deviation) and the sum of the stent cell size from both original and re-sampled phantom data set. The stent cell size and MCUSA from the original phantom data set are treated as the ground truth, so that the errors for the 3D stent cell surface, 2D stent cell approximation and MCUSA from the re-sampled data set can be computed.

Data set	Feature	Max (mm^2)	Min (mm^2)	Mean ± SD (mm^2)	Sum (mm^2)	Error (%)
Original Phantom data set (ground truth)	Full stent cell size	5.74	3.96	4.75 ± 0.44	71.27	--
	MCUSA	1.70	0.95	1.29 ± 0.22	19.28	--
Re-sampled Phantom data set (algorithmic results)	Stent cell surface	5.64	3.97	4.72 ± 0.44	70.77	0.96 ± 0.64
	2D app-roximation	5.74	3.99	4.79 ± 0.45	71.90	0.98 ± 0.74
	MCUSA	1.70	0.87	1.25 ± 0.22	18.76	5.0 ± 5.2

Table 2. The maximum, minimum, mean value (with standard deviation) and the sum of the stent cell surface size, 2D stent cell approximation size and MCUSA size in 12 in-vivo IVOCT data sets.

Data set	Feature	Max (mm^2)	Min (mm^2)	Mean ± SD (mm^2)	Sum (mm^2)
In-vivo IVOCT pullback runs	Stent cell surface	10.04	1.00	3.01 ± 1.39	328.06
	2D approximation	9.55	1.07	3.10 ± 1.34	337.38
	MCUSA	1.40	0.25	0.96 ± 0.80	104.21

Table 3. The maximum, minimum and mean size (with standard deviation) of the side branch access from the original and re-sampled phantom data sets and in-vivo IVOCT data sets. The sum of the side branch access equal to the sum of side branch lumen areas. The amount of side branches and the stent cells in front of side branches and the percentage of the average maximum side branch access comparing to the average side branch lumen in every group are also given.

Data set	Max (mm^2)	Min (mm^2)	Mean (mm^2)	Sum (mm^2)	Side branch amount	Cell amount	Max access (%)
Original phantom	2.30	0.23	0.86 ± 0.86	12.83	4	21	53.69
Re-sampled phantom	2.39	0.26	0.89 ± 0.88	13.46	4	21	53.31
In-vivo IVOCT data sets	4.21	0.22	0.68 ± 0.49	31.06	27	46	77.59

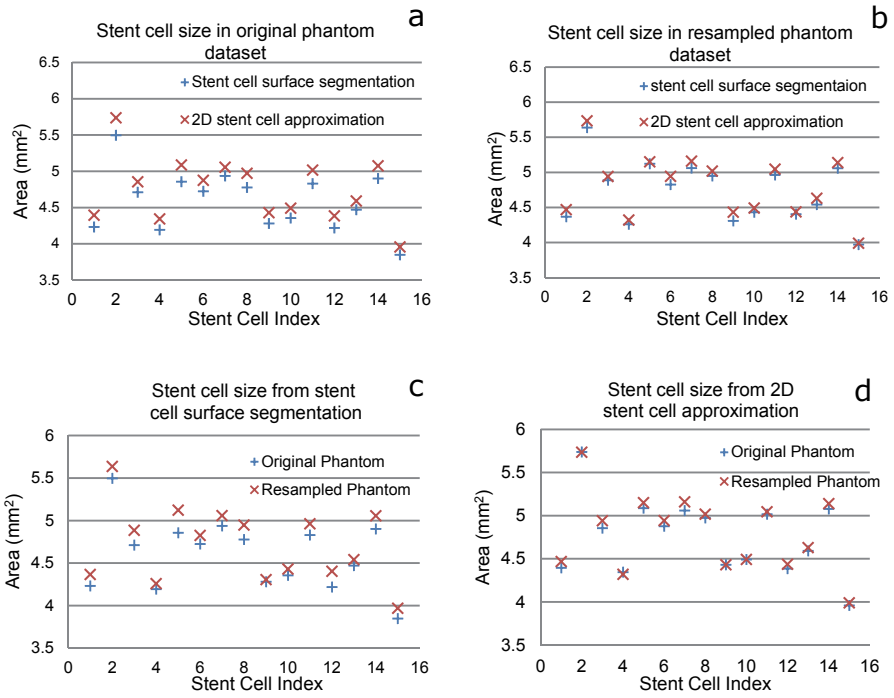

Figure 4-8. (a) shows the results of 3D stent cell surface and 2D stent cell approximation in the original phantom data set, while (b) shows these results from the re-sampled phantom data set. (c) indicates the results of 3D stent cell surface in both original and re-sampled phantom data sets, while chart (d) compares the corresponding size of 2D stent cell approximation in both original and re-sampled phantom data sets.

4.5 Discussion

To validate the accuracy of the presented approach, the relative errors of our algorithmic results were computed. The mean and the standard deviation of the relative errors were determined to demonstrate the performance. Table 1 shows that the ground truth of the whole stent surface area is 71.27 mm^2 and the sum of the MCUSA is 19.28 mm^2. In the re-sampled phantom data set, the estimated stent surface size is 70.77 mm^2 from the summation of 3D stent cell surfaces and 71.90 mm^2 from the summation of 2D stent cell approximations, while the summation of the MCUSA is 18.76 mm^2. Compared to the ground truth, the average error of the every 3D stent cell surface is 0.96 ± 0.64%, while that of the 2D stent cell approximation is 0.98 ± 0.74% and the MCUSA error is 5.0 ± 5.2%. In the re-sampled phantom data sets, the 3D stent cell surface and 2D stent cell approximation results are almost the same as the ground truth like Fig. 8 (a) and (b) show. It suggests that our approach is very accurate when measuring the stent cell size within the resolution of in-vivo IVOCT pullback runs. Fig. 8 (c) and (d) demonstrate that the stent cell surface size is usually a little bit smaller

than the 2D stent cell approximation size. A possible explanation is that the stent cell surface is segmented from the reconstructed stent surface that consists of thousands of small triangles, while the 2D stent cell approximation calculates the stent cell using the opened surface from the fitted cylinder. For a curved surface, the opened surface should be bigger than the surface that is approximated with triangle polygons.

Table 2 shows the quantitative analysis results of 105 stent cells from 12 clinical IVOCT pullback runs. The mean difference between the 3D stent cell surfaces and 2D approximations is 4.2 ± 2.3%. Since the distributed stent struts do not fit to any regular shape in 3D space, we could not obtain the ground truth of in-vivo stent cell areas. However, our methods provide an intuitive approximate measurement of the stent cell size in clinical data sets.

According to Table 3, the experimental results of the side branch access through stent cells in both original and re-sampled phantom data sets indicate that the average error of the algorithmic results is 8.9 ± 7.0%. For the in-vivo IVOCT pullback runs, more than 60% of the side branches have more than one stent cell ostia. On average, the largest ostium includes more than 77.6% of the side branch lumen area, and the sum of the largest two ostia includes 92.6% of the lumen area. By contrast, the numbers in the phantom data set with un-extended cells are smaller as 53.1% and 75.9%. The experimental results clearly show that, in most of our in-vivo cases, the stents cells in front of side branches have been extended so that side branches are less covered. The only exception is the BVS stent, because compared to bare metal and drug-eluting stents, BVS stents are less flexible and can break easier. Consequently, in the BVS data set, one side branch is covered by 6 stent cells while another side branch has 3 stent cells and none of the stent cells are extended.

IVOCT image sequences provide the longitude image data of the implanted stent along the imaging catheter. In practice, the imaging catheter may be curved. Without the 3D tracking of the imaging catheter, the cell area in IVOCT data may contain an error when the imaging catheter bends. However, in most cases, the trajectory of the imaging catheter has only very smooth curvatures so that the error for distortion is limited. Therefore, this method is expected to give a good approximation of the stent cell area. This method requires only stent strut positions for stent surface reconstruction and stent cell indication. Therefore, it is available for any type of bare metal stents, drug-eluting stents or BVS stents. With provided struts and side branches information, it can compute the MCUSA and side branch access for any stents.

If a side branch is fully or partly covered by the guide wire shadow or a bridge, this side branch will not be detected or measured, since its contour is incomplete. The same situation could happen for stent cells and these cells cannot be indicated or measured as well. Imaginary struts can be added to assist the stent surface reconstruction, but if more than half of the stent is covered or unclear, the reconstructed stent surface is less reliable for assessment. In most of our cases, guide wire shadow regions cover less than a quarter of the stent contour and the imaginary struts are concentrated only in the shadow region. Hence the reconstructed stent surface can be separated as real surface part and imaginary surface part. Imaginary part will not affect the shape of the real surface part and the measurement is applied only on the real surface part. The presented side branch detection method could fail if the lumen contour appears like a highly narrowed ellipse, because the distal lumen can be missed due to the limited penetration (< 2 mm) of IVOCT [23]. In these special cases, a manual correction is requested.

The side branch projection should follow the angle between the side branch and the main vessel. However, due to the limited penetration of IVOCT, the angle of the side branch cannot be measured. Therefore, in the presented method, the projection direction is always vertical to the center-line of the stent. For stent cell contours and side branch contours, we chose different projection methods. Theoretically, the projection method for side branches should be the optimal way. However, the projection of stent cells will introduce only tiny error but is much time efficient. The stent cell surface results are accurate enough and the computing is easy and fast.

During the IVOCT acquisition, some artifacts may arise as results of many different reasons. Some artifacts like residual blood noise [31] and the sun-flower artifact [23] were mostly removed during our processing, while many artifacts were not taken into account in this research, such as non-uniform rotational distortion (NURD) [32], because the new frequency-domain IVOCT system has a very fast speed to reduce these artifacts.

4.6 Conclusion and future work

With its high resolution, IVOCT allows a better understanding of the stent structures in the coronary arteries. We have presented an approach to measure the stent support degree and the side branch access in IVOCT pullback runs. It detects stent struts, reconstructs stent cells, generates 2D stent cell approximations, detects stent-covered side branches and reconstructs the irregular stent surface for MCUSA and side branch access assessment. A full resolution phantom data set and its re-sampled data set were used to evaluate the feasibility and the accuracy of this approach. Next, it was applied to twelve in-vivo IVOCT data sets. Quantitative evaluation reveals that the approach has achieved high accuracy for the MCUSA and side branch access measurement. The results suggest that this method can be a useful tool for the stent implantation improvement, stent design evaluation, blood flow analysis and computer-guided diagnosis. There are still artifacts that may affect the results of the presented method, and we will work on that in future.

4.7 References

1. Bosiers M, de Donato G, Deloose K, Verbist J, Peeters P, Castriota F, et al. Does free cell area influence the outcome in carotid artery stenting? European Journal of Vascular and Endovascular Surgery 2007;33(2):135-141.

2. Tanigawa J, Barlis P, Dimopoulos K, Dalby M, Moore P, Di Mario C. The influence of strut thickness and cell design on immediate apposition of drug-eluting stents assessed by optical coherence tomography. International Journal of Cardiology 2009;134(2):180-188.

3. Takebayashi H, Mintz GS, Carlier SG, Kobayashi Y, Fujii K, Yasuda T, et al. Nonuniform strut distribution correlates with more neointimal hyperplasia after sirolimus-eluting stent implantation. Circulation 2004;110(22):3430-3434.

4. Mejia J, Ruzzeh B, Mongrain R, Leask R, Bertrand OF. Evaluation of the effect of stent strut profile on shear stress distribution using statistical moments. Biomedical Engineering Online 2009;8.

5. Trivisonno A, Musumeci G, Sirbu V, Lortkipanidze N, Matiashvili A, Mihalcsik L, et al. Strut Number and Distribution: Implications for Drug-Eluting Stent Coverage and Neointimal Growth. In-vivo Insight from Optical Coherence Tomography. American Journal of Cardiology 2008;102(8A):145I.

6. Unal G, Gurmeric S, Carlier SG. Stent implant follow-up in intravascular optical coherence tomography images. International Journal of Cardiovascular Imaging 2010;26(7):809-816.

7. Capelli C, Gervaso F, Petrini L, Dubini G, Migliavacca F. Assessment of tissue prolapse after balloon-expandable stenting: Influence of stent cell geometry. Medical Engineering & Physics 2009;31(4):441-447.

8. Conti M, Van Loo D, Auricchio F, De Beule M, De Santis G, Verhegghe B, et al. Impact of Carotid Stent Cell Design on Vessel Scaffolding: A Case Study Comparing Experimental Investigation and Numerical Simulations. Journal of Endovascular Therapy 2011;18(3):397-406.

9. Cremonesi A, Setacci C, Castriota F, Valgimigli M. Carotid stent cell design: Lack of benefit or lack of evidence? Stroke 2008;39(8):E130.

10. Okamura T, Garg S, Gutierrez-Chico JL, Shin ES, Onuma Y, Garcia-Garcia HM, et al. In vivo evaluation of stent strut distribution patterns in the bioabsorbable everolimus-eluting device: an OCT ad hoc analysis of the revision 1.0 and revision 1.1 stent design in the ABSORB clinical trial. Eurointervention 2010;5(8):932-938.

11. Lee JB, Kim KS, Kim SY, Lee YS, Ryu J, Choi JY, et al. Comparison of nonuniform strut distribution among three drug-eluting stent platforms. American Journal of Cardiology 2008;101(8B):72C.

12. Suzuki Y, Ikeno F, Yeung A. Drug-Eluting Stents strut distribution; A comparison of 3 stent designs by optical coherence tomography. American Journal of Cardiology 2005;96(7A):182H.

13. O'Brien CC, Finch CH, Barber TJ, Martens P, Simmons A. Analysis of Drug Distribution from a Simulated Drug-Eluting Stent Strut Using an In Vitro Framework. Annals of Biomedical Engineering 2012;40(12):2687-2696.

14. Onuma Y, Serruys PW. Bioresorbable Scaffold The Advent of a New Era in Percutaneous Coronary and Peripheral Revascularization? Circulation 2011;123(7):779-797.

15. Gomez-Lara J, Brugaletta S, Diletti R, Garg S, Onuma Y, Gogas BD, et al. A comparative assessment by optical coherence tomography of the performance of the first and second generation of the everolimus-eluting bioresorbable vascular scaffolds. European Heart Journal 2011;32(3):294-304.

16. Ruffino MA, Rabbia C. Endovascular Repair of Peripheral and Visceral Aneurysms With the Cardiatis Multilayer Flow Modulator: One-Year Results From the Italian Multicenter Registry. Journal of Endovascular Therapy 2012;19(5):599-610.

17. Mortier P, De Beule M, Van Loo D, Verhegghe B, Verdonck P. Finite element analysis of side branch access during bifurcation stenting. Medical Engineering & Physics 2009;31(4):434-440.

18. Rizik DG, Hermiller JB, Klassen KJ, Shah M. Xience Side Branch Access Stent for Treatment of Bifurcation Coronary Disease: A Review of Preclinical Data. Journal of Interventional Cardiology 2012;25(4):337-343.

19. Kurisu S, Mitsuba N, Kato Y, Ishibashi K, Dohi Y, Nishioka K, et al. External Side-Compression of Radial Artery: A Simple Technique for Successful Advancement of Guidewires through the Radial Approach. Journal of Interventional Cardiology 2011;24(5):397-400.

20. Burzotta F, De Vita M, Sgueglia G, Todaro D, Trani C. How to solve difficult side branch access? Eurointervention 2010;6:J72-J80.

21. Abtahian F, Jang IK. Optical coherence tomography: basics, current application and future potential. Current Opinion in Pharmacology 2012;12(5):583-591.

22. Hamdan R, Gonzalez RG, Ghostine S, Caussin C. Optical coherence tomography: From physical principles to clinical applications. Archives of Cardiovascular Diseases 2012;105(10):529-534.

23. Wang A, Eggermont J, Dekker N, Garcia-Garcia HM, Pawar R, Reiber JH, et al. Automatic stent strut detection in intravascular optical coherence tomographic pullback runs. Int J Cardiovasc Imaging 2013;29(1):29-38.

24. Tsantis S, Kagadis GC, Katsanos K, Karnabatidis D, Bourantas G, Nikiforidis GC. Automatic vessel lumen segmentation and stent strut detection in intravascular optical coherence tomography. Med Phys 2012;39(1):503-513.

25. Mandelias K, Tsantis S, Karnabatidis D, Katsakiori P, Mihailidis D, Nikiforidis G, et al. Fast and Robust Algorithm Towards Vessel Lumen and Stent Strut Detection in Optical Coherence Tomography. Medical Physics 2012;39(6):3645-3646.

26. Gurmeric S, Isguder GG, Carlier S, Unal G. A new 3-D automated computational method to evaluate in-stent neointimal hyperplasia in in-vivo intravascular optical coherence tomography pullbacks. Med Image Comput Comput Assist Interv 2009;12(Pt 2):776-785.

27. Fitzgibbon A, Pilu M, Fisher RB. Direct least square fitting of ellipses. Ieee Transactions on Pattern Analysis and Machine Intelligence 1999;21(5):476-480.